sustainability

MDPI

Article

Holistic Dynamic Modeling of Open-Cathode PEM Fuel Cells for Sustainable Hydrogen Propulsion in UAVs

Teresa Donateo *, Andrea Graziano Bonatesta and Antonio Ficarella

Department of Engineering for Innovation, University of Salento, 73100 Lecce, Italy; andreagraziano.bonatesta@unisalento.it (A.G.B.); antonio.ficarella@unisalento.it (A.F.)
* Correspondence: teresa.donateo@unisalento.it; Tel.: +39-0832-297-754

Abstract

The adoption of proton exchange membrane fuel cells (PEMFCs) in unmanned aerial vehicles (UAVs) offers a sustainable pathway to zero-emission propulsion, supporting aviation decarbonization by replacing battery or fossil fuel systems with efficient hydrogen technology. This work presents the development, validation, and application of a comprehensive dynamic model of a 1 kW open-cathode PEMFC system, including complete balance of plant (BOP) and control logic for four cooling fans, a purge valve, and a short-circuit unit (SCU). The model was validated through extensive experiments with step, triangular, and real-world UAV current profiles. Under steady-state conditions, it reproduces stack voltage with a <1 V average error and a temperature of 2.5 °C. Dynamic modeling accurately predicts fan behavior, purge/SCU events, and transient voltage drops. Applied to a 25 min UAV flight, the model quantifies reactant-management impacts: purge events increase H_2 usage by 4.8%, with SCU raising total to 5.6% above stoichiometric consumption. Altitude analysis shows ambient temperature reduction dominates the oxygen partial pressure effects, yielding net cell voltage increase under current-based fan control. These insights underscore explicit BOP and ambient modeling for accurate UAV endurance estimation and strategy optimization, providing a basis for future altitude-chamber validation. By enabling precise BOP dynamics simulation and H_2 optimization, this model advances the achievement of affordable clean energy, facilitating an extended endurance with minimal environmental impact.

Keywords: sustainable aviation; hydrogen decarbonization; unmanned aerial vehicles (UAVs); open-cathode fuel cell; dynamic modeling; balance of plant (BOP); purging; short-circuit unit

Academic Editor: Vittorio Di Vito

Received: 26 November 2025
Revised: 16 December 2025
Accepted: 18 December 2025
Published: 23 December 2025

1. Introduction

The hydrogen economy represents one of the most promising routes toward sustainable energy and propulsion systems, directly supporting the Sustainable Development Goals of the United Nations: in particular, SDG 7 (affordable and clean energy), through efficient conversion and SDG 13 (climate action) via zero-emission aviation [1,2].

Initially, fuel cells were adopted in aircraft as auxiliary power units; however, in recent years, their application has extended to the electric propulsion of drones and small aerial vehicles, often in combination with batteries and, occasionally, supercapacitors [3]. Due to the high energy density of hydrogen and the elevated specific power of proton exchange membrane fuel cells (PEMFCs), such systems can achieve lower take-off weights and longer flight endurance, compared with battery-only configurations [4]. In comparison with

hydrogen-fueled internal combustion engines, fuel cells offer higher energy conversion efficiency while emitting only water vapor.

For small-scale applications, such as drones with power demands below approximately 6 kW, air-cooled open-cathode configurations are typically adopted. In these systems, the same airflow simultaneously supplies oxygen to the cathode and removes heat from the stack. The conversion of hydrogen into electrical energy requires appropriate management of the reactants, effective thermal control to maintain an optimal stack temperature, and voltage regulation through an electronic control system. Membrane humidification is controlled by means of a dedicated water management circuit [5] or a short-circuiting device [6]. These auxiliary subsystems, collectively referred to as the balance of plant (BOP) [7], consume parasitic power from the stack during normal operation and from the battery during start-up.

The typical architecture of a self-humidified PEM fuel cell system for unmanned aerial vehicles (UAVs) is illustrated in Figure 1. Hydrogen pressure and flow rate are regulated via a control valve, while the anode commonly operates in a dead-end mode. In this configuration, a purge valve is periodically opened to remove the accumulated water and impurities, which are expelled along with a small fraction of hydrogen. Water buildup at the anode results from back diffusion from the cathode [8]; the resulting pressure difference promotes a hydrogen flow that clears excess water, thereby maintaining cell performance and preventing deep voltage drops. The purge frequency and duration must be optimized to limit voltage losses below approximately 100 mV, ensuring effective water management [9] while minimizing hydrogen consumption [10]. Bradley et al. [11] noted that this purging strategy penalizes the overall powertrain efficiency at part load, although, to the best of the authors' knowledge, a quantitative assessment of this effect, as performed in the present investigation, is not yet available in the literature. Air is supplied by one or more fans powered by the stack during normal operation and by the battery during start-up. The stack temperature is regulated by modulating fan speed, which in turn adjusts the airflow rate. External humidification is unnecessary, owing to the self-humidification mechanism, which is commonly implemented in commercial open-cathode PEM fuel cells through an integrated short-circuit unit (SCU).

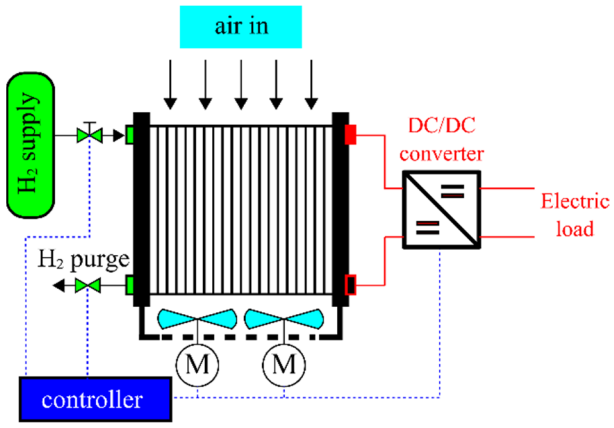

Figure 1. Balance of plant of a self-humidified OCPEMFC.

Commercial PEM fuel cells employ the short-circuit method to increase the proton conductivity of the membrane by promoting additional water generation. During a short-circuit event, a transient overcurrent flows through the stack, significantly accelerating the hydrogen–oxygen reaction rate and thereby increasing water production. Furthermore, short-circuiting can improve catalyst activity by removing oxide layers that form on platinum surfaces because of sluggish oxygen diffusion kinetics at the cathode [6]. SCU control

strategies are often implemented by system integrators or fuel cell manufacturers without a comprehensive understanding of the underlying physical mechanisms or the associated secondary effects. Some studies have reported that repeated short-circuit operation may accelerate performance degradation [12]. In addition, the use of a short-circuit unit (SCU) can negatively influence hydrogen consumption, which has been observed to increase considerably, particularly at low-load conditions [13]. However, the available literature on this topic remains limited [14], especially for open-cathode PEMFC systems, where the stack's operating temperature is also affected by the short-circuiting process, as observed in the present investigation.

Rapid variations in load and altitude during flight have a significant influence on the performance of aeronautical PEMFCs [15]. Increasing flight altitude leads to reductions in air temperature and density, which in turn affect fan behavior. When a sudden rise in load is experienced, the gas diffusion layers of the cell cannot supply hydrogen or oxygen fast enough because of the response delay of the balance of plant (BOP). This leads to reactant starvation, which can cause cell voltage reversal, carbon corrosion, catalyst degradation, and irreversible damage to the membrane, ultimately reducing the overall PEMFC performance and lifespan [16]. To properly capture these phenomena, both the dynamic response of the fuel cell and that of its BOP must be modeled accurately.

Fuel cell modeling approaches can be classified according to the level of analysis, the degree of model complexity, and the treatment of dynamic effects. Regarding the level of analysis, single-cell and stack models typically focus on the voltage–current characteristics, whereas system-level models address temperature control via fan operation and the management of the purge valve.

Based on the underlying physics and computational effort, models are generally divided into three main categories: black-box, gray-box, and white-box models [17]. In black-box models, experimental input–output data are correlated without explicit consideration of the underlying physical processes. Such data-driven models—including fuzzy logic and artificial neural networks—have been applied, for example, to temperature control in PEMFC systems [18]. They are characterized by high predictive accuracy within a specific operating range and by low computational cost, making them suitable for real-time parameter identification [17]. However, their lack of physical insight limits their general applicability.

White-box, or mechanistic, models [19–21] are based on algebraic and/or differential equations that explicitly describe the electrochemical, thermodynamic, and fluid-dynamic processes. These models are well suited for investigating the influence of geometrical and operational parameters on cell performance. Gray-box models combine physical relationships with experimental data, offering a compromise between computational efficiency and physical fidelity. For this reason, they are often considered the most appropriate solution for energy management and control purposes [17].

The dynamic behavior of a fuel cell system under variable load conditions can be investigated through either quasi-static or fully dynamic modeling approaches [22]. In quasi-static models, variations in load and boundary conditions are assumed to occur slowly, relative to the intrinsic system dynamics, such that the fuel cell operates under quasi-equilibrium conditions. Consequently, quasi-static simulations represent a sequence of steady-state operating points along the mission profile. Their main objective is to evaluate PEMFC voltage–current characteristics under slow load changes, often using equivalent electrical circuit models consisting of resistive and capacitive elements. MATLAB/Simulink is the most common simulation environment for such analyses [23], although alternative numerical tools are also employed [24].

Dynamic models, in contrast, are used to test control strategies and to analyze the transient response of the fuel cell to rapid load variations [25]. In hybrid electric powertrains incorporating fuel cells, quasi-static system models are generally sufficient; nevertheless, the thermal dynamics of the PEMFC must be considered in the development of energy management strategies [17], particularly for small drones operating under rapidly changing loads and altitudes [26,27]. Nevertheless, recent works in the scientific literature still use current–voltage relationships for the design and management of fuel-cell-powered UAVs [28,29].

The influence of altitude on open-cathode PEMFC performance has received limited attention in the literature on aerospace applications, as previously highlighted by [30]. For unmanned aerial vehicle (UAV) applications, Atkinson et al. [31] demonstrated that PEMFCs can operate across wide ranges of temperature, relative humidity, airspeed, and altitude. Nonetheless, their study reported a noticeable reduction in maximum power output during flight, which was attributed to increases in ambient humidity (up to 24%), flight speed (up to 28%), and elevation (up to 20%).

More recently, Mus et al. [32,33] analyzed the combined influence of ambient temperature and humidity on the net stack power, also accounting for the parasitic consumption of the fans. The main effects of altitude on the overall PEMFC system, as discussed in [30], are summarized in Table 1, where they are categorized according to their significance (negligible, minor, major).

Table 1. Effects of ambient conditions on PEMFC performance.

Component	Parameter	Ambient Temperature	Ambient Pressure	Ambient Humidity
Stack	Nernst voltage		***	*
	Activation losses		**	
	Ohmic losses		*	**
	Concentration losses		*	
Cooling system	Air flow rate and PWM duty cycle	***	***	**
	Fan power	***	***	*
Purging system	Hydrogen utilization	*	***	*

* Negligible effect, ** minor effect, *** major effect.

Goal, Novelty Claim, and Organization of the Paper

The goal of the present investigation is to present a comprehensive simulation tool to support the design and energy management of hybrid UAV powertrains.

Based on the review of the available literature presented in [30] and updated in this study, it emerges that no comprehensive dynamic model currently exists that simultaneously captures all relevant transient phenomena and the influence of altitude on open-cathode PEMFCs performance. The aim of the present investigation is to address this gap by developing and validating a dynamic model for a 1 kW open-cathode PEMFC system, including its complete balance of plant (BOP).

The model is designed as a system-level tool to predict the major effects of ambient conditions on the overall behavior and performance of the open-cathode PEM fuel cell system. It incorporates key balance of plant elements, including temperature control, fan operation, and management of the purge and short-circuit valves.

This modeling approach addresses the sustainability gaps by quantifying BOP parasitic losses (e.g., purge/SCU increasing H_2 use by 5.6%) and altitude effects, enabling optimized energy management for hybrid UAV powertrains that minimize hydrogen waste and maximize flight efficiency, which is critical for scaling low-carbon aerial applications.

The main contributions of this work can be summarized as follows:

- Development of a comprehensive dynamic model that incorporates heat transfer within the stack, the parasitic power consumption of the fans, the influence of purging on fuel cell performance, and the effects of short-circuit operation on both stack voltage and hydrogen consumption.
- Design and implementation of an experimental setup enabling full characterization of an open-cathode stack, together with its BOP.
- An original state-machine model for purging and short-circuit operations.
- Model validation through an extensive experimental campaign, including tests performed under a real-world power demand profile acquired from a UAV quadcopter.
- Quantitative assessment and modeling of the impact of purge and short-circuit operations on hydrogen consumption and overall flight endurance.
- Evaluation of altitude effects on the performance and efficiency of the fuel cell system.

The originality of the present contribution does not lie in the individual sub-models for stack voltage, temperature, fan flow rate, and purge, which are largely based on established formulations. Rather, it stems from their seamless integration into a unified, system-level simulation framework. The only new sub-model introduced in this paper relates to the short-circuiting action. To the authors' knowledge, no dynamic model of the short-circuit unit (SCU) has yet been proposed in the literature, while in this work, an empirical model for short-circuiting is adopted, inspired by the purge modeling approach of Ishaku et al. [34].

The proposed integrated approach enables a holistic analysis of fuel cell system dynamics under realistic operating conditions, including variable loads and changing environmental factors. For instance, Ishaku et al. [34] account for purging and temperature dynamics but do not represent the short-circuit action, nor do they quantify the effect of purging on the global efficiency of the fuel cell system. Mahjoubi et al. [35] propose and validate a dynamic model of the stack and its BOP, but do not model the mass flow rate of hydrogen.

By contrast, the proposed framework allows for performance metrics such as efficiency, degradation-related indicators, and hydrogen consumption to be evaluated more accurately than with simplified models. This capability supports the optimized design and control of PEM fuel cell systems in demanding applications, such as UAV propulsion.

The remainder of the paper is organized as follows. Section 2 describes the experimental setup and the design of the tests used to characterize the fuel cell system and generate the validation dataset. Section 3 presents the structure of the dynamic model, detailing the electrochemical, thermal, and balance of plant sub-models together with the implemented control logics for the fans, purge valve, and short-circuit unit. Section 4 reports the validation of the model under both steady-state and dynamic operating conditions, including the reproduction of a real UAV power profile. Section 5 illustrates the application of the model to UAV-relevant scenarios, with a particular focus on hydrogen consumption and altitude effects. Section 6 underlines the model limitations that will be addressed in the continuation of the project. Finally, Section 7 summarizes the main conclusions and outlines the directions for future work.

2. Experimental Setup and Tests

The experimental test bench implemented to characterize an open-cathode fuel cell system (FCS) is depicted in Figure 2. A programmable electronic load is employed to impose various profiles of current or load. The data acquisition system records the principal stack parameters—namely, current, voltage, and temperature—via the stack's serial communication port. The stack temperature is obtained from a single thermocouple, located almost at the center of the stack.

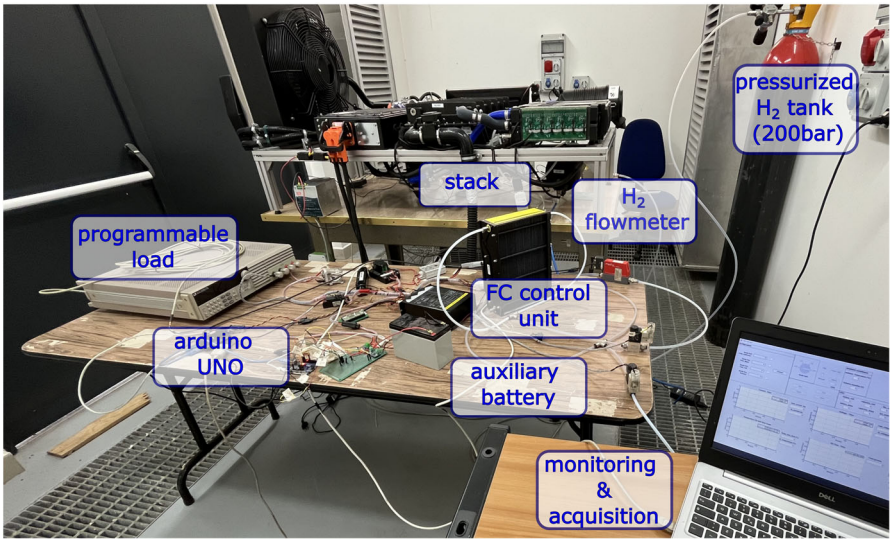

Figure 2. Experimental setup.

In addition, the platform monitors the fan and supercapacitor electrical signals, fan rotational speed, and the ambient temperature, pressure, and relative humidity. These signals are acquired through a custom Arduino-based system. The hydrogen mass flow rate and temperature are measured through a flowmeter connected via its serial interface. All measurement devices are synchronized and managed through a dedicated computer-based control system. The complete list of acquired variables, along with the corresponding sampling frequency and measurement accuracy, is provided in Table 2.

Table 2. Details of the experimental setup.

Measured Variable	Accuracy	Acquisition Frequency	Source
Stack Temperature	0.5 °C	1 Hz	Stack serial port
Stack voltage	0.333 V	1 Hz	Stack serial port
Stack current	0.2 A	1 Hz	Stack serial port
Hydrogen mass flow	0.001 g/min	1 Hz	Flowmeter serial port
Temperature H_2 inlet	0.1 ° C	1 Hz	Flowmeter serial port
Voltage Fan (INA219)	3.9 mV	1 Hz	Arduino-USB
Current Fan (INA219)	0.05 mA	1 Hz	Arduino-USB
Fan speed	1 rpm	1 Hz	Arduino-USB
Voltage capacitor bank (voltage divider)	0.05 V	1 Hz	Arduino-USB
Current capacitor bank (ACS712-20A)	0.05 A	1 Hz	Arduino-USB
Humidity ambient	1%	1 Hz	Arduino-USB
Temperature ambient	0.1 °C	1 Hz	Arduino-USB
Load voltage	0.01 V	1 Hz	Arduino-USB
Load current	0.01 A	1 Hz	Arduino-USB

The PEMFC analyzed in this investigation has a nominal power of 1 kW and comprises four cooling fans, a start-up battery, a purge valve, a hydrogen pressure regulator, and a control unit. Note that the system is not specifically designed for application to UAV but for another application requiring fast load changes. The main technical specifications of the FCS are summarized in Table 3, while the polarization curve of the stack is shown in Figure 3. Other details of the system cannot be reported here because of a confidentiality agreement.

Table 3. Main specifications of the fuel cell system.

Category	Value
Type of fuel cell	PEM
Number of cells	50
Active area	50 cm^2
Peak power	1100 W
Stack mass	4.9 kg
Rated current	0–33.5 A @30 V
DC voltage	25–48 V
H_2 purity	99.99%
H_2 relative pressure	0.5–0.65 bar
External temperature	5–35 °C
Max stack temperature	65 °C
Humidification	Self-humidified
Relative humidity	10–95%
Air cooling	4 × fan 80 × 25 mm 13.8 VDC
Start-up battery	Lead acid 12 V

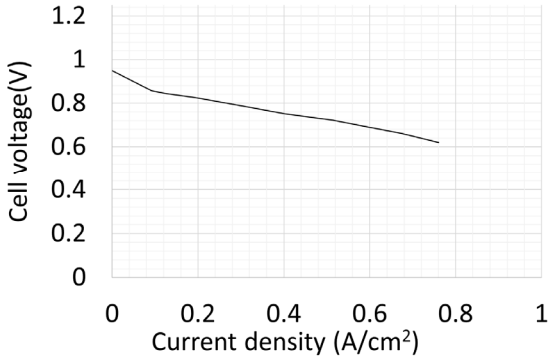

Figure 3. Polarization curve of the cell (extrapolated by the manual at 24 °C and RH = 35%).

At higher altitudes, the reduction in air density affects both the heat dissipation and oxygen supply, thereby influencing the overall performance of the UAV propulsion system. To investigate these effects, the entire experimental setup has been designed for integration within an altitude chamber, enabling the analysis of the PEMFC system under simulated flight conditions up to an altitude of 2000 m. However, at the current stage of the research, this facility, shown in Figure 4, is not yet available for experimental testing.

Figure 4. Altitude chamber.

Design of Experiments

The input signals applied during the experimental tests for model validation are presented in Figure 5. Ambient temperature and relative humidity (RH) were recorded for each test, conducted during the spring–summer period in Lecce, and are also reported in Figure 5.

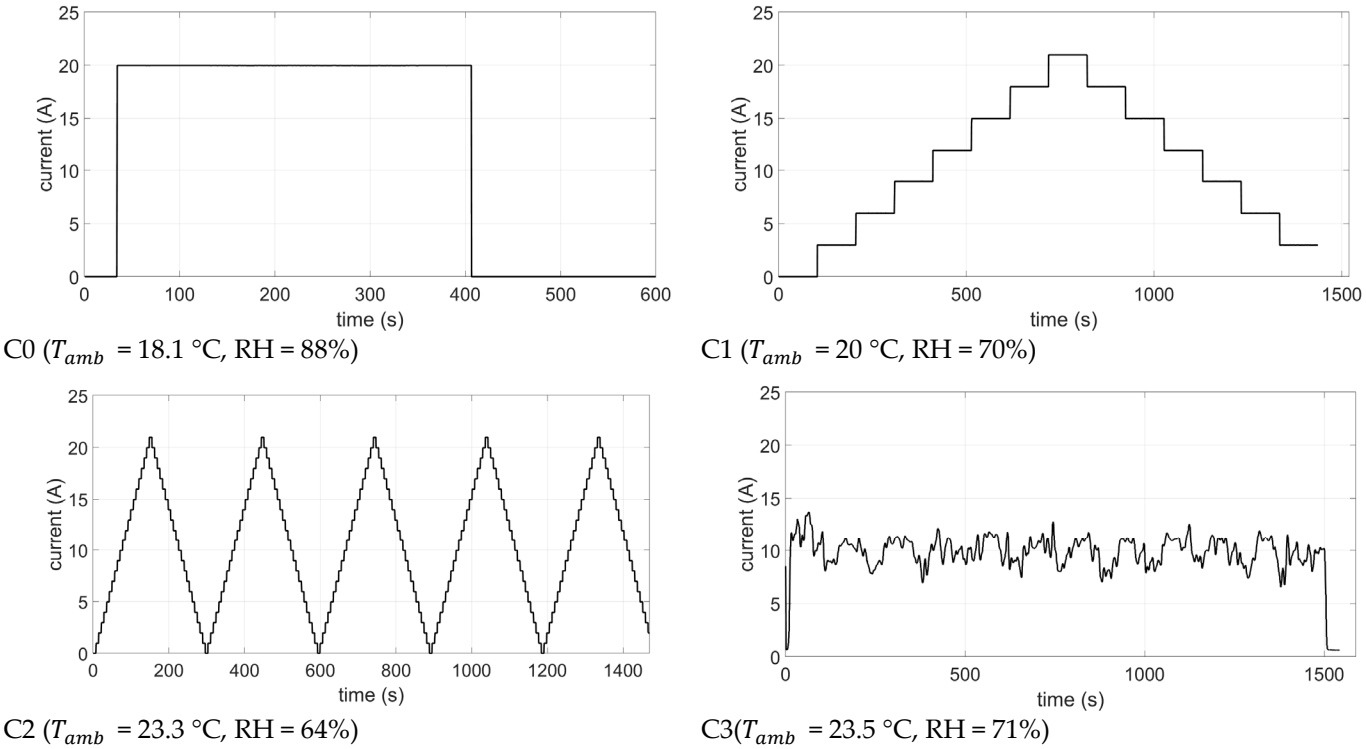

Figure 5. Input signals for the tests.

Test C0 employed a square current waveform, stepping from 0 A to 20 A and then back to 0 A after 400 s. This test was designed to evaluate the dynamic response of the fuel cell system.

In Test C1, the current was incrementally increased and decreased in 100 s steps, allowing the stack to reach quasi-stationary thermal conditions. The objective of this test was to determine the steady-state values of voltage, temperature, and other key parameters as a function of the load current, like the fan speed. The test was repeated nine times and was performed with and without the activation of the SCU.

Test C2 applied a triangular current waveform, gradually increasing and decreasing the current so that the stack never reached steady-state conditions during the test.

In Test C3, the current profile, recorded from a Dronebase eXplorer 1000 during a 25 min flight at an altitude of approximately 200 m, was reproduced. The **DroneBase eXplorer** is a tactical drone designed and manufactured by **DroneBase S.r.l., Rimini, Italy.**

All tests were conducted with the stack, initially at ambient conditions, simulating a "cold start" scenario. The duration of all tests, except C0, was 1500 s to match the length of the recorded flight profile. It should be noted that, due to the inherent variability of the ambient conditions, which strongly influence the FCS performance, each test was performed only once, except for Test C1, which was repeated six times to characterize steady-state operation at different current levels. More comprehensive testing will be conducted once the altitude chamber becomes available.

Figure 6a compares the steady-state polarization curve from test C1 to the manufacturer's declared data. The manufacturer provides two polarization curves at different temperatures and humidity levels to illustrate performance variability under varying ambient conditions. Black error bars represent variability across the nine repeated tests with the same input profile; this variability is minimal and barely visible, except at currents between 15 A and 20 A. As shown in Figure 6b, the stack temperature under steady-state operation rises nearly linearly with the current. The variability of the temperature is also quite limited, except for the temperature obtained at 15 A.

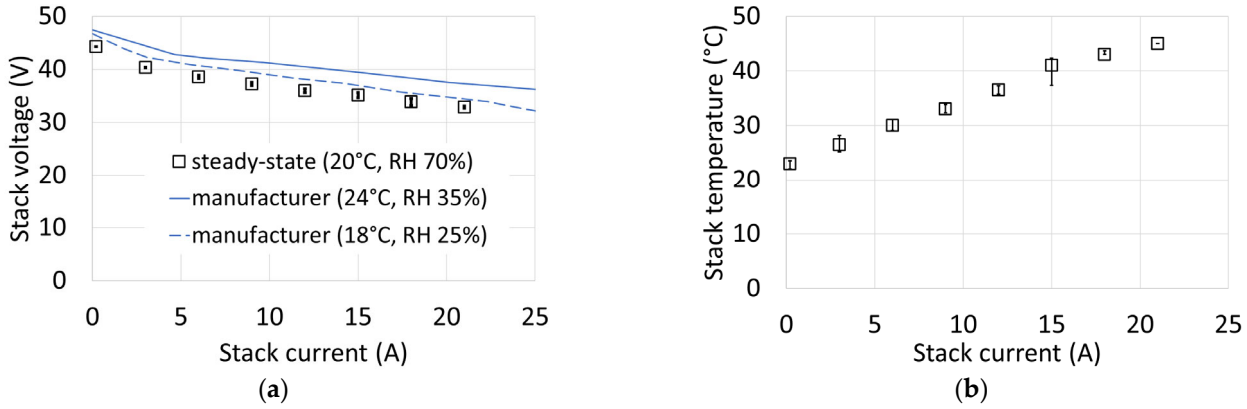

Figure 6. Estimated steady-state voltage–current (**a**) and temperature–current (**b**) curves, with error bars.

3. Modeling the Fuel Cell System

The goal of the modeling activity is to reproduce the behavior of the fuel cell at sea level under dynamic operation and to estimate the effect of the ambient values of temperature, pressure, and humidity. These effects cannot be captured by a model based only on current–voltage relationships, as is often used in the scientific literature for the sizing and management of fuel cell systems for UAV [28]. To this scope, the proposed system-level model incorporates temperature control, fan operation, and valve management functions.

After a detailed analysis of the state of the art on the dynamic modeling of open-cathode PEMFCs [30], the dynamic model shown in Figure 7 was implemented using the R2024a Matlab/Simulink. The model consists of five interconnected main blocks:

(1) Power balance.
(2) Cathode control.
(3) Anode control.
(4) Thermal balance.
(5) Performance and plots.

The model requires the following main input signals:

- The required load demand of current or power vs. time.
- The altitude vs. time.
- Measured pressure, temperature, and humidity of ambient air (if available, otherwise standard ISA conditions are considered).

The model also requires suitable control logic for the fan speed, the opening of the purge valve, and operation of the SCU.

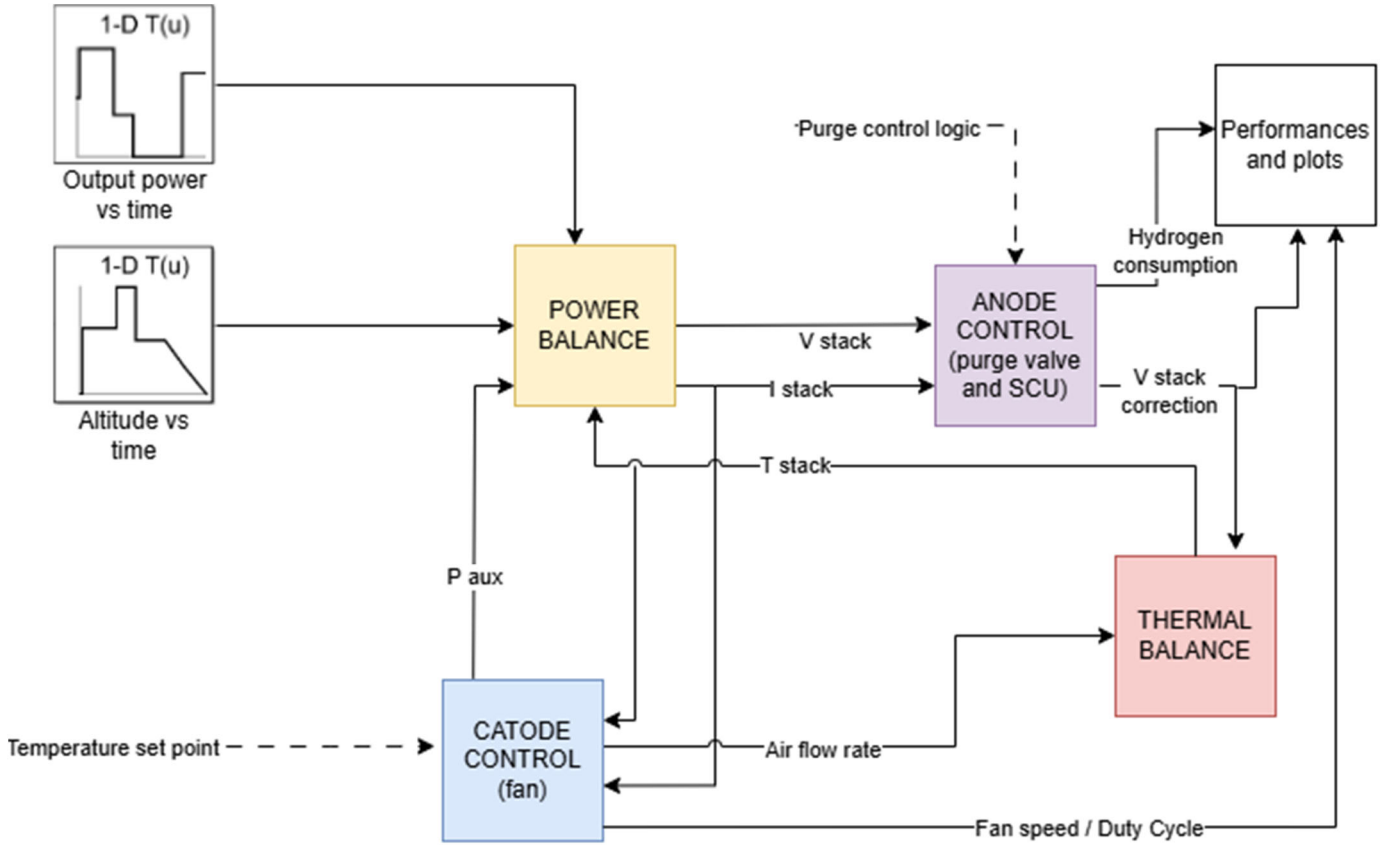

Figure 7. Main flow chart of the dynamic model.

3.1. The Power Balance Block

This block determines the fuel cell voltage to meet the load request and estimates the parasitic power of the balance of plant.

The voltage of the stack, V_{st}, is calculated as follows [7]:

$$V_{st} = N(E_{Nernst} - \Delta V_{ohm} - \Delta V_{act} - \Delta V_{conc} + \Delta V_{SCU}) \quad (1)$$

where N is the number of cells in series. The other symbols are explained one by one in the following text.

E_{Nernst} is the reversible open circuit of the electrochemical cell associated with the change in Gibbs energy in the global reaction $H_2 + \frac{1}{2}O_2 \rightarrow H_2O + heat$. E_{Nernst} is calculated as the sum of three contributions:

$$E_{Nernst} = E_0 + E_1 + E_d \quad (2)$$

The first term E_0 is the available voltage that depends only on the stack temperature, T_{st}:

$$E_0 = 1.229 - 0.85 \times 10^{-3}(T_{st} - 298.15) \quad (3)$$

The second term takes the effect of the partial pressure of hydrogen P_{H_2} and oxygen P_{O_2} into account, [7]:

$$E_1 = 4.3085 \times 10^{-5} T_{st} \cdot \left(\ln(P_{H_2}) + \frac{1}{2}\ln(P_{O_2}) \right) \quad (4)$$

The partial pressure of oxygen can be obtained from the cathode pressure, which includes oxygen, nitrogen, and water vapor partial pressures, with the following equation [36]:

$$P_{O_2} = P_c - RH_c P_w^{sat} - P_{N_2} \exp\left(0.291 \frac{\frac{I_{st}}{S_{act}}}{T_{stack}^{0.832}}\right) \quad (5)$$

where P_c is the cathode pressure, $P_{N_2} = \frac{0.79}{0.21} P_{O_2}$ is the partial pressure of nitrogen, RH_c is the relative humidity in the cathode channel, and P_w^{sat} is the saturation pressure of water vapor at the operating temperature:

$$\log_{10}(P_w^{sat}) = 2.95 \times 10^{-2}(T_{st} - 273.15) - 9.18 \times 10^{-5}\left(T_{st} - 273.15\right)^2 \quad (6)$$

The last term, E_d, takes into account the influence of the flow of hydrogen and oxygen delays on output voltage during load transient. It can be modeled as proposed by Li et al. [37]:

$$E_d = \lambda_{din}(1 - I_{st}(t)\exp(-t/\tau_e)) \quad (7)$$

In this equation, τ_e is the overall flow delay and λ_{din} is a constant factor [24].

The voltage drop caused by irreversibility is expressed as the sum of the ohmic (ΔV_{ohm}), activation (ΔV_{act}), and concentration (ΔV_{conc}) voltage drop.

The activation loss was modeled with the Tafel equation [7]:

$$\Delta V_{act} = \frac{RT_{st}}{2\alpha F} ln\left(\frac{I_{st}}{S_{act}\ I_0}\right) \quad (8)$$

where α is the transfer coefficient and I_0 is the exchange current. R and F are the ideal gas constant and the Faraday constant, respectively.

The exchange current is a function of oxygen partial pressure [38]:

$$I_0 \propto (pO_2)^y \quad (9)$$

where y is the reaction order with respect to oxygen partial pressure, usually assumed to be equal to one.

Ohmic losses are modeled as follows:

$$\Delta V_{Ohm} = R_{Ohm} I_{st} \quad (10)$$

The ohmic resistance, R_{ohm}, is inclusive of the resistance of the proton-conducting membrane, catalyst layer, and electrodes through which the protons and electrons are transported. A constant value is assumed in this analysis. However, the ohmic resistance is affected by membrane humidity and stack temperature and, therefore, is lower when the SCU is activated. This is evident from the experimental signals of voltage in Figure 8, where the nine repetitions (one to nine) of C1 with the SCU off are reported together with the test with SCU on. To account for the effect of the SCU, a different value of the internal resistance is considered for the test, with and without the activation of the SCU. However, a more advanced model for the relationship between the water content and ionic resistance, like that proposed by [39], will be implemented when the tests are repeated with controlled humidity and temperature conditions, due to the adoption of the altitude chamber.

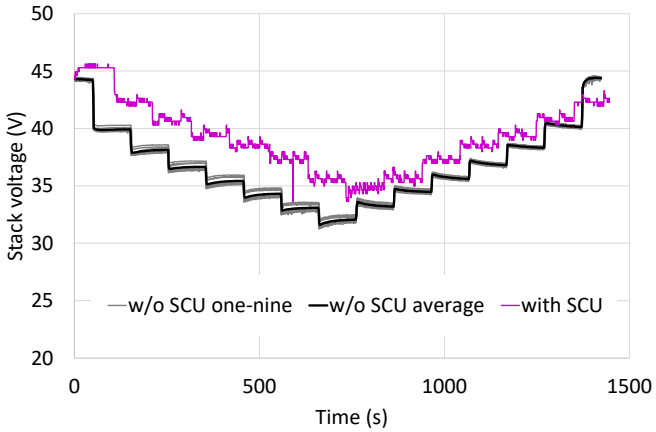

Figure 8. Effect of the SCU on the stack voltage (test C1).

The loss of voltage caused by mass transport is modeled with the exponential equation:

$$\Delta V_{conc} = -\frac{\beta RT_{st}}{2F} \ln\left(1 - \frac{I_{st}}{I_{max}}\right) \quad (11)$$

where I_{max} is the limit current, set equal to 50 A, and β is treated as a fitting parameter [30]. However, this type of loss is negligible for the tests performed in this investigation, since the current never exceeds 21 A.

With SCU activation in Figure 8, the voltage is not only, on average, higher than in the case without SCU, but it shows an overshoot at each short-circuit event, followed by a subsequent decrease caused by impurity accumulation. The semi-empirical model by Hou et al. [40] was applied here to quantify the voltage drop from impurities between consecutive short-circuit events:

$$\Delta V_{SCU} = -k_{SCU} \cdot \ln(t - t_1) \quad (12)$$

where t_1 is the starting time of the purge event.

3.2. The Thermal Balance Block

The stack temperature is calculated using the following differential equation:

$$\frac{dT_{st}}{dt} = \frac{1}{m_{FC} C_{FC}} (\dot{Q}_{gen} - \dot{Q}_{nat} - \dot{Q}_{rad} - \dot{Q}_{fan} - \dot{Q}_{sens+lat}) \quad (13)$$

where m_{FC} is the mass of the stack and C_{FC} is its thermal capacity. The heat produced from the exothermic chemical reaction can be computed as $\dot{Q}_{gen} = (E_{nernst} \cdot N - V_{st}) \cdot I_{st}$.

$\dot{Q}_{nat}$ is the heat flux dissipated by the fuel cell surface by means of natural convection with the external environment $\dot{Q}_{nat} = h_{nat} \cdot S_{nat} \cdot (T_{st} - T_{amb})$, with h_{nat} and S_{nat} being the convective heat transfer coefficient and the heat transfer area, respectively. The contribution of radiation, $\dot{Q}_{rad}$, was neglected in the implementation, as suggested in the scientific literature.

The forced convection in the cathode side, generated by the fan, can be calculated as follows:

$$\dot{Q}_{fan} = \dot{m}_{air} c_{p,air} (T_{st} - T_{amb}) \quad (14)$$

where $\dot{m}_{air}$ is the air flow rate that is assigned in the fan control block.

$\dot{Q}_{sens+lat}$ is the sensible and latent-heat-associated water warming and phase change [41]. The latent heat, $\dot{Q}_{l/g}$, is given by the following:

$$\dot{Q}_{l/g} = \rho_w \frac{NR}{4P_a F} T_{st} L_w I_{st} k_w \quad (15)$$

where ρ_w is the water density, L_w is the latent heat of evaporation, k_w is an empirical coefficient representing the rate of water produced in liquid form that evaporates, and P_a is the anode pressure.

3.3. The Cathode Control Block (Fan)

This block defines the fan speed and the corresponding flow rate of air $\dot{m}_{air}$, which are used for the reaction and for cooling. The fan speed control is implemented as a 1D look-up table, being mainly dependent on the stack current in the simulated fuel cell system. The lookup table obtained under steady-state operation is reported in Table 4.

Table 4. Set points for the fan speed.

Current Interval (A)	Fan Speed (rpm)
0–7	2330
7–15	2800
15–22	3250

Under dynamic operation, the fan speed depends on the stack temperature, in addition to the stack current. When the measured stack temperature exceeds the set-point value by a significant margin, the control unit increases the fan speed to prevent overheating [32]. As a result, for the same current level, the fan speed is generally higher during current decreases than during current increases, and this hysteresis behavior is consistent with the experimental observations reported in [33].

To represent this behavior, the fan-speed control under dynamic conditions is modeled by applying a correction to the steady-state set points of Table 4. Specifically, the fan speed is driven to its maximum value (6000 rpm) when the difference between the stack temperature and its set point exceeds 20 °C. The temperature set points adopted for this control strategy are summarized in Table 5.

Table 5. Set points for the stack temperature.

Current Interval (A)	Stack Temperature (°C)
0–5	40
5–10	42
10–20	45
20–30	50

The cathode control block also calculates the fan's parasitic power by using a polynomial correlation obtained by interpolating the experimental data, as shown in Figure 9:

$$P_{fan} = (1.69{\cdot}10^{-10} n_{fan}^3 - 7.08{\cdot}10^{-7} n_{fan}^2 + 3.74{\cdot}10^{-3} n_{fan}) \frac{\rho_a(z)}{\rho(s.l.)} \quad (16)$$

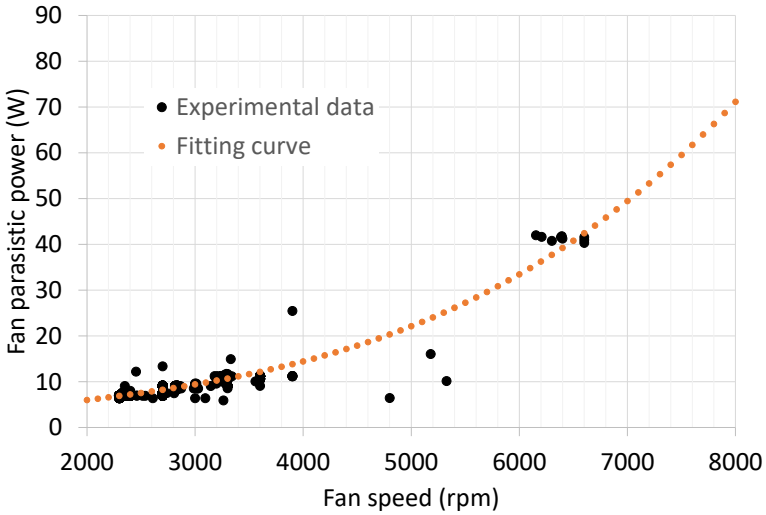

Figure 9. Parasitic power vs. fan's speed, as measured during the tests and fitting curve.

The term $\frac{\rho_a(z)}{\rho(s.l.)}$ is used to correct the absorbed power with the air density at altitude z, while $\rho(s.l.)$ is the density of the atmospheric air at sea level. Note that P_{fan} includes the losses in the DC-DC converter, calculated from the signals of current and voltage acquired on the fans' motor.

The inertia of the fan-motor is neglected, since the experimental data show that the dynamic of the fan speed is very fast compared to the dynamic of the temperature in the stack.

The large dispersion in fan parasitic power is attributed to other losses and dynamic effects in terms of shaft speed that are not accounted for in this investigation. Note that the fan's parasitic power is inclusive of losses associated not only with the fan but also with the motor and the DC-DC converter. However, at the moment, we are not able to separate these effects.

3.4. The Anode Control Block (Purge Valve and SCU)

The cell converts the chemical energy of hydrogen into electricity with the following overall reaction:

$$H_2 + \frac{1}{2}O_2 \rightarrow H_2O + 286\ \text{kJ/mol} \tag{17}$$

From the stoichiometry of this reaction, the block calculates the mass flow rate of hydrogen that reacted, $\dot{m}_{H_2,\,react}$:

$$\dot{m}_{H_2,\,react} = \frac{M_{H_2}}{2F} \cdot I_{st} \tag{18}$$

where M_{H_2} is the molar mass of hydrogen.

However, the actual consumption of hydrogen is higher because of the dynamic issues and losses related to the dead-end operation. The additional consumption of hydrogen is accounted for by introducing the utilization factor, UF [7].

The anode control block replicates the opening law of the purge valve of the selected fuel cell in terms of the duration and frequency of the purge action, by means of the finite state machine shown in Figure 10. In particular, test C1 was used for the tuning of the time between two consecutive purge events: purge period t_p, and the opening timing of the purge valve, Δt_{open} , were found to be a function of the stack current, as reported in Table 6.

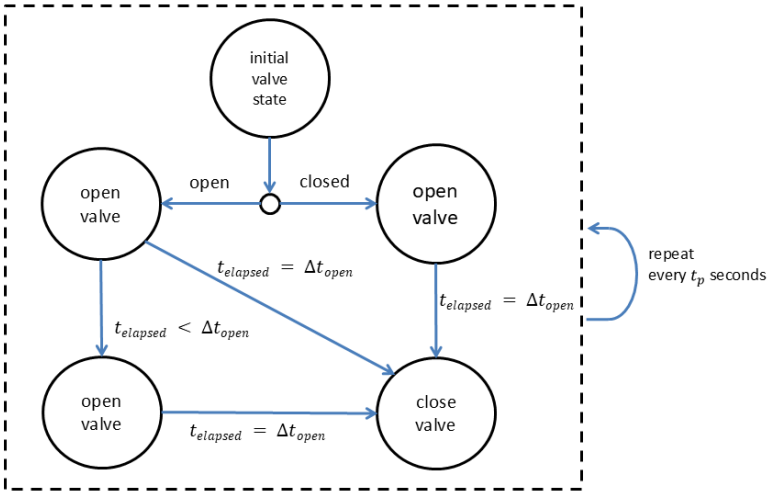

Figure 10. Finite state machine for the opening of the purge valve.

Table 6. Details of the purge control law.

Current Interval (A) I_{st}	Purge Period (s) t_p	Purge Valve Opening Time(s) t_{open}
0–7	500 s	6 s
7–14	100 s	6 s
14–16	60 s	7 s
16–18	40 s	7 s
18–20	30 s	7 s
20–22	30 s	8 s

The block also calculates the loss of hydrogen through the purging valve. This is a critical and non-negligible aspect. Bradley et al. [11] measured an average hydrogen purge flow rate of about 1 L/min in a 500 W stack, obtaining a hydrogen utilization factor that increased with current from 0.26 to 0.9.

In the present investigation, the flow rate of hydrogen obtained from Equation (18) is corrected with the following equation, which is a simplified version of the model suggested by [34]:

$$\dot{m}_{H_2}(t) = \dot{m}_{H_2,react} + \left(\dot{m}_{H_{2,max}} - \dot{m}_{H_{2,react}}\right) \cdot \left(1 - \exp\left(-\frac{t - t_1}{\tau_p}\right)\right) \quad (19)$$

where $\dot{m}_{H_{2,max}}$ is the maximum purge flow rate and the nominal flow rate, while τ_p is the time constant of the mass flow rate dynamics.

A similar approach is used to model the behavior of the stack when the short-circuit unit is activated, since it was observed that the SCU causes spikes similar to those of the purge valve, but with a higher frequency and lower intensity, as shown in Figure 11, where the mass flow rates recorded in the nine repetitions without SCU are depicted in gray. In the case of the SCU being on, purge-related spikes match those without SCU in both frequency and magnitude. Note that SCU operation, the magenta line, presents smaller spikes during short-circuiting, which are more pronounced and impactful at low currents.

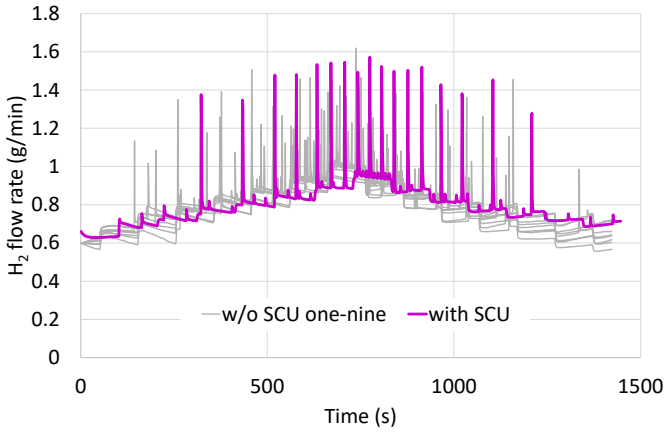

Figure 11. Effect of the SCU on the hydrogen flow rate.

To model the activation of short-circuiting, a second finite state machine was implemented for replicating the opening time and frequency of the SCU, and Equation (19) was applied again with a lower value of $\dot{m}_{H_{2,max}}$. The frequency and duration of the short circuiting are reported in Table 7.

Table 7. Details of the SCU control law.

Current Interval (A)	Short Circuit Period (s) t_s	Short Circuit Duration (s) Δt_{scu}
0–7	60	3
7–10	60	3
10–16	30	3.5
16–18	20	3.5
18–20	10	3.5
20–22	10	4

As pointed out by Lin et al. [42], the hydrogen mass flow rate depends on the ratio between anode pressure and ambient pressure, since the valve can be modeled as a restriction. Therefore, it is expected to increase with altitude, since the hydrogen pressure can be considered to be almost constant while the ambient pressure decreases with altitude.

$$\dot{m}_{H_{2,max}} \propto \sqrt{\frac{P_a}{P_{amb}(z)} - 1} \tag{20}$$

where P_a is the anode pressure and $P_{amb}(z)$ is the atmospheric pressure.

3.5. The Performance and Plots Block

The gross power of the cell is calculated as follows:

$$P_{gross} = V_{st} I_{st} \tag{21}$$

Part of the gross power is used to power the fans through the DC-DC converter and the fuel cell control unit. The net power of the fuel cell is estimated here as follows:

$$P_{net} = V_{st} I_{st} - P_{fan} \tag{22}$$

The ratio between the net power and the chemical power is the overall efficiency or net efficiency of the fuel cell:

$$\eta_{net} = \frac{P_{net}}{\dot{m}_{H_2} LHV} \tag{23}$$

where LHV is the lower heating value of hydrogen.

The stack efficiency is estimated as follows:

$$\eta_V = \frac{V_c}{1.25} \tag{24}$$

where V_c is the cell voltage and 1.25 V is the available electromotive force.

4. Results of the Validation

This section describes the validation of the model under stationary and dynamic operating conditions.

4.1. Validation Under Steady-State Operation

The quasi-static experimental data were obtained from test #C, at the end of each transient step-up and -down. The plots of Figure 12 show the comparison between the measured values and the model in terms of stack voltage (a) and temperature (b), with the same layout. The measured values correspond to the average values of Figure 6.

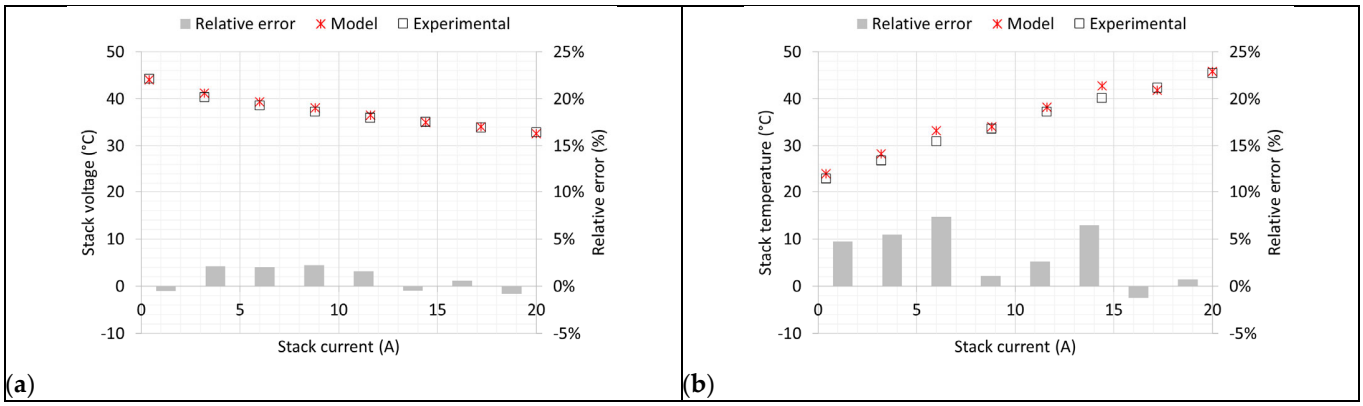

Figure 12. Results of the validation under steady-state operation in terms of stack voltage (**a**) and temperature (**b**).

The piecewise behavior of the modeled stack temperature is due to the discretized nature of the fan control, which is based on Table 4.

The model captures very well both the voltage and temperature's dependence on the current. The absolute error for voltage is below 1 V and 2.5 °C for temperature. The relative errors are shown in the plots.

Figure 13a compares the data of hydrogen consumption obtained with the simulation code and the experiments, while Figure 13b reports the curves of efficiency vs. current. The voltaic and net efficiencies were calculated with Equations (24) and (23), respectively. Unfortunately, the flowmeter used for the investigation presents a drift in the data, as evident from the very high mass flow rate, about 0.6 g/min, measured at no load. Moreover, the error bars show a higher uncertainty for the experimental data, compared with voltage and temperature. Even if this could be partly due to the necessity of powering auxiliaries, the measured value is too high when compared with similar studies. After verifying the lack of losses of hydrogen in the whole hydrogen line and in the stack, the authors concluded that this could be caused by sensor degradation. For this reason, Figure 13b does

not show the net efficiency for the experimental data. The acquisition of a new flowmeter has already been implemented in the altitude chamber and will be used for the continuation of the project.

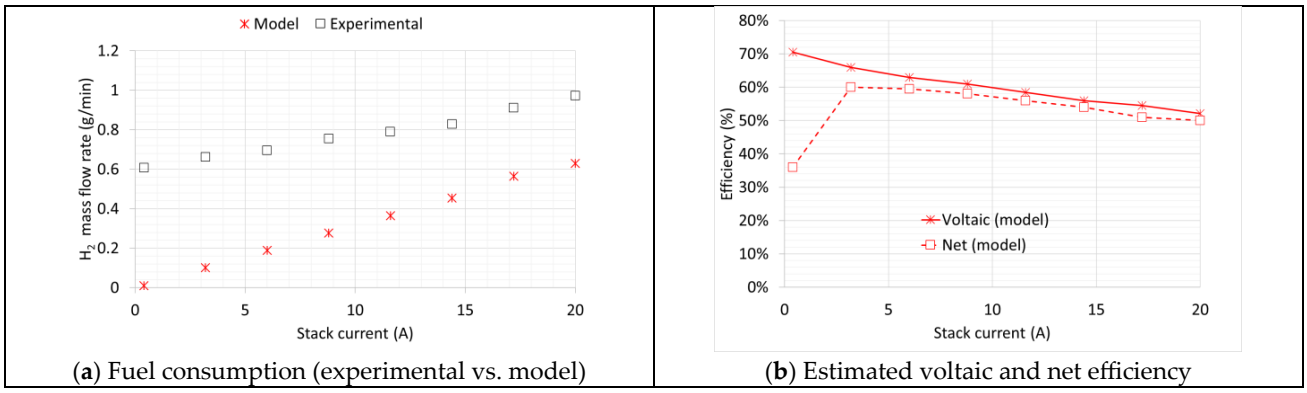

(**a**) Fuel consumption (experimental vs. model) (**b**) Estimated voltaic and net efficiency

Figure 13. Performances of the stack under stationary operating conditions.

Note that the voltaic efficiency is strictly proportional to the stack voltage shown in Figure 12. The net efficiency is, on average, 3% lower than the voltage efficiency for currents higher than 6 A, while at a low load, it is much lower because of the effect of the parasitic power of the fan. In fact, the parasitic power of the fan amounts to 62% and 8% of the stack gross power at 0.4 A and 3 A, respectively.

4.2. Dynamic Analysis

The voltage and temperature signals recorded from the fuel cell stack during the experimental tests depicted in Figure 5 are presented in Figures 14 and 15, respectively. Additionally, a comparative analysis of fan speed during these tests is shown in Figure 16. These three parameters—stack voltage, stack temperature, and fan speed—are inherently coupled under dynamic operating conditions and thus warrant a joint discussion.

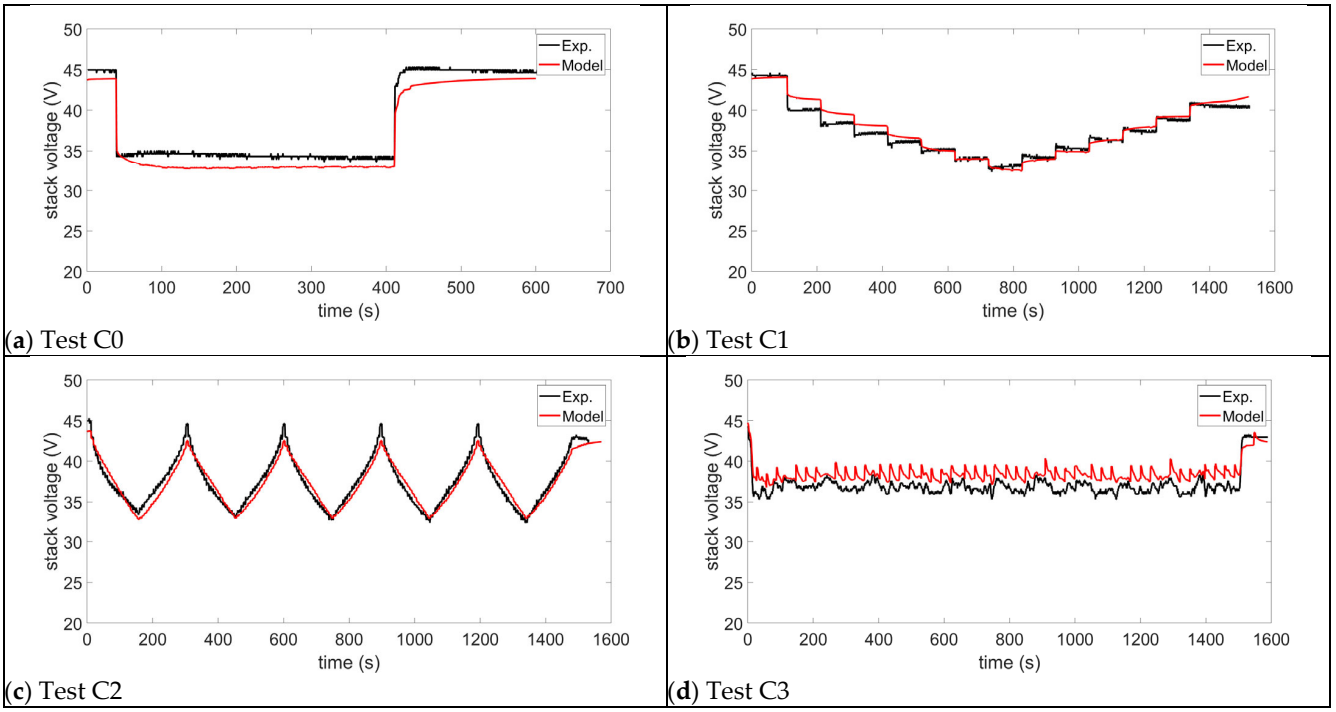

(**a**) Test C0 (**b**) Test C1

(**c**) Test C2 (**d**) Test C3

Figure 14. Results of the validation under dynamic operation without SCU: stack voltage.

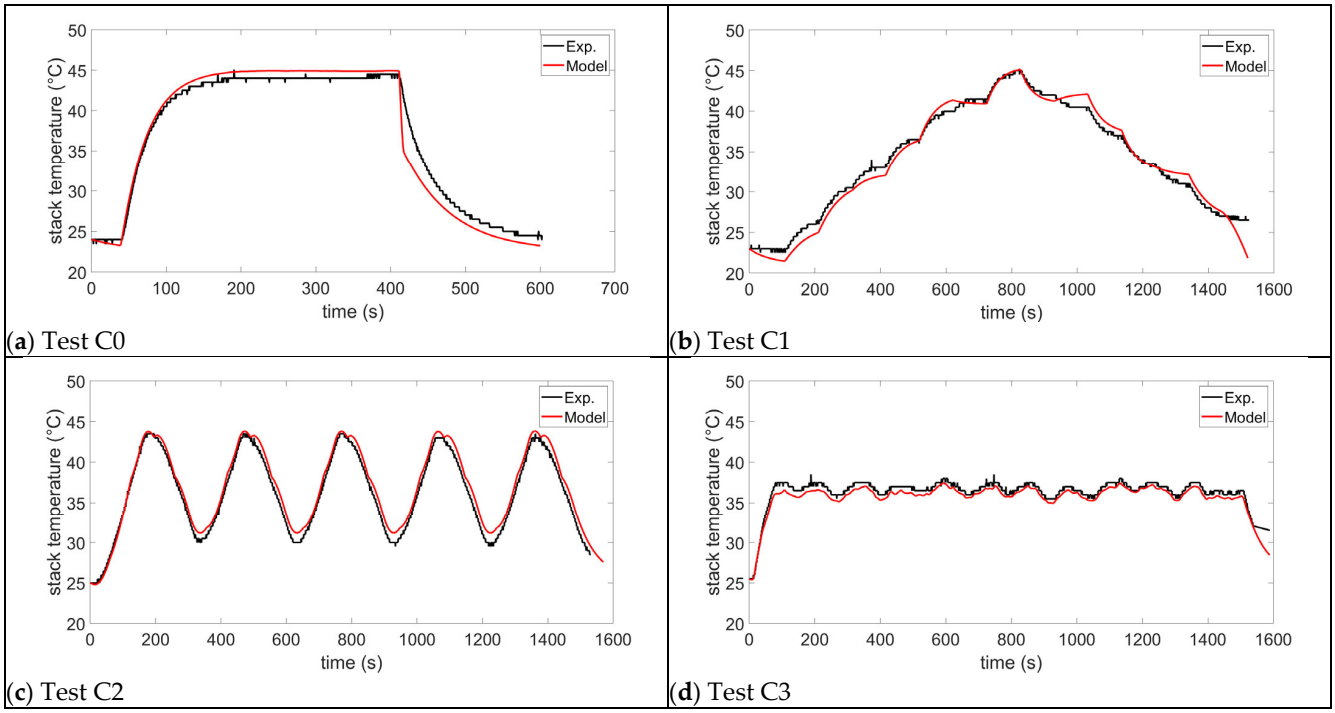

Figure 15. Results of the validation under dynamic operation without SCU: stack temperature.

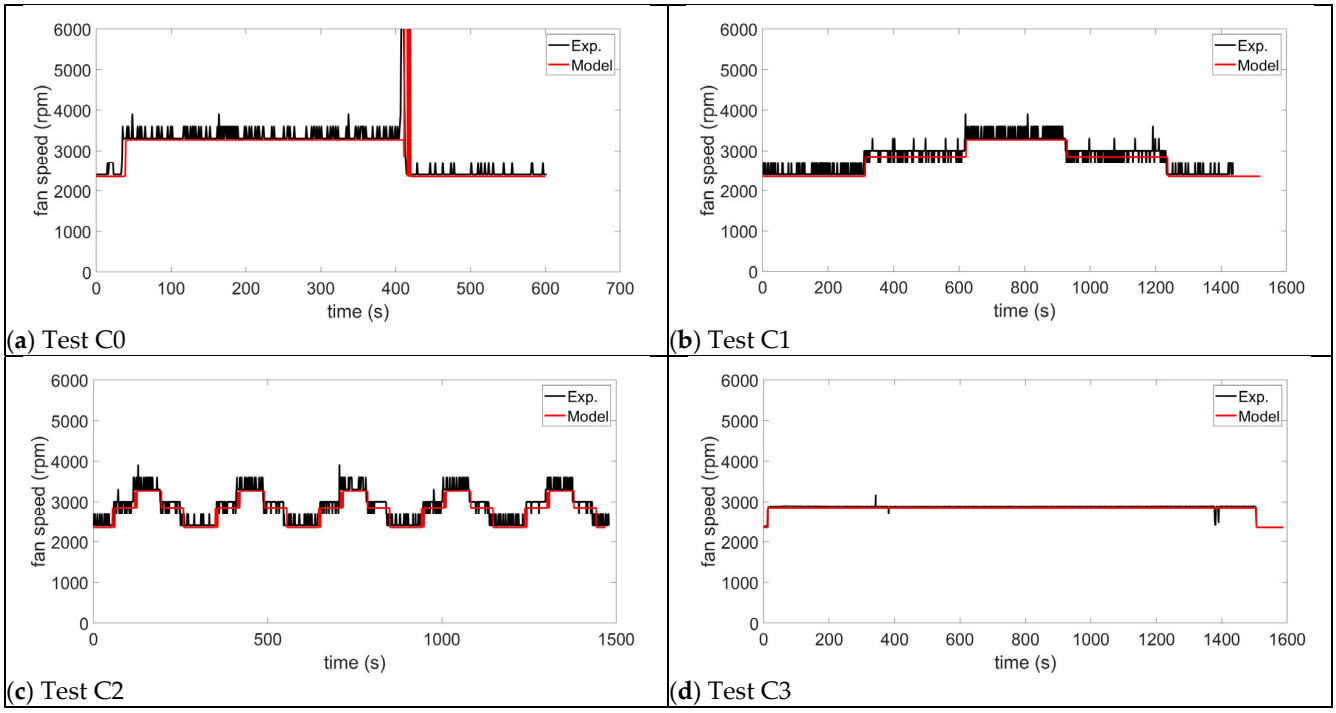

Figure 16. Results of the validation under dynamic operation: fan speed, without SCU.

In dynamic operation, stack voltage and temperature exhibit a strong interdependence. The stack temperature directly influences the Nernst voltage through temperature-dependent terms, as outlined in Equations (3) and (4). It also affects activation losses, which are described by Equation (8). Conversely, the stack voltage contributes to the thermal state of the stack through the heat generation term in Equation (13), which forms part of the thermal balance equation. The stack temperature is further modulated by the convective cooling driven by the air mass flow rate, which is controlled via the fan speed. Since the

thermal and electrical behaviors of the stack are so closely intertwined, understanding their mutual influence is essential for accurate modeling and control.

The fan speed is captured accurately across all experimental tests, as Figure 16 shows, indicating that the model's prediction of the air mass flow rate $\dot{m}_{air}$—used in the thermal balance through Equation (14)—is reliable. Therefore, the small discrepancies observed in the stack temperature data in Figure 15 cannot be attributed to errors in the fan speed or air flow modeling. Instead, the observed underprediction of the stack temperature at higher current levels during test C2 correlates with a slight overestimation of the stack voltage, which leads to an overestimation of the reaction heat generation. This highlights the sensitivity of the thermal predictions to the electrical model's accuracy.

Despite these minor discrepancies, the model successfully captures the overall dynamic temperature behavior, particularly for test C2, which is characterized by rapid load current variations. This good agreement suggests that the thermal capacity of the stack assumed in the model, $m_{FC}C_{FC} = 750\frac{J}{K}$, is reasonably accurate and can effectively reflect transient thermal responses. However, temperature predictions, particularly at no load conditions observed during the first 30 s of tests C0 and C1, could be further improved by refining the natural convection coefficient. The thermal model calibration process will benefit greatly from the additional testing performed under carefully controlled ambient conditions to reduce external variability.

The voltage prediction during stepwise load changes, such as those in tests C0 and C1, exhibits less accuracy. Specifically, the model struggles to replicate the voltage undershoot and overshoot phenomena occurring immediately after load steps. This limitation indicates that the current formulation of Equation (7) needs further refinement to better capture these transient voltage dynamics. Improving this aspect of the model could enhance the accuracy of the voltage predictions under rapidly changing load conditions and contribute to more robust control strategies for the fuel cell system.

The observed discrepancies in the average voltage can be attributed to additional dynamic effects that are not fully captured by the current model. In particular, variations in the stack's humidity—an important parameter influencing electrochemical performance—are not directly measured during the tests and therefore remain unaccounted for in the model. Moreover, the accumulation of impurities within the stack, which can degrade performance over time, is only approximated, rather than explicitly modeled. These unmeasured and approximated phenomena introduce uncertainties that contribute to the differences between predicted and experimental voltage signals.

Despite these limitations, the accuracy of the proposed model remains consistent with that reported in comparable studies within the scientific literature [10,34,35]. This level of agreement demonstrates the robustness of the modeling approach while highlighting areas where future refinements, such as incorporating real-time humidity measurements or more detailed impurity dynamics, could enhance the predictive fidelity.

The model is also accurate in predicting the effect of the SCU activation in terms of voltage and temperature (Figure 17) and, in particular, the spikes in the voltage curve highlighted the experimental data, previously shown in Figure 8.

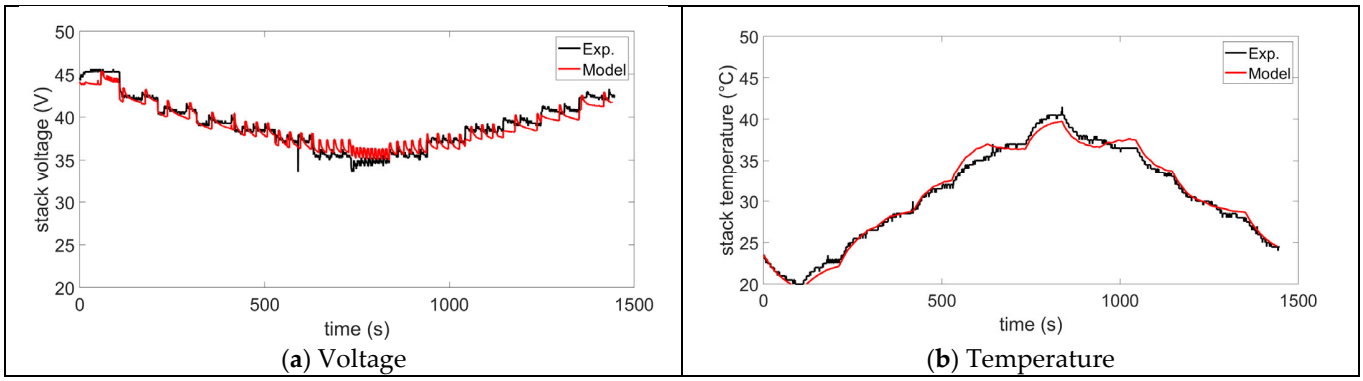

(**a**) Voltage (**b**) Temperature

Figure 17. Results of the validation under dynamic operation: stack voltage and temperature with SCU for test C2.

4.3. Purging Model Tuning and Validation

The values of t_p and Δt_{open} of Table 6 were obtained by fitting the position of the spikes in the first repetition of test C1, which is reported in black in Figure 18. The resulting mass flow rate of hydrogen predicted by the model is depicted in red. The zoom plot shows the detail of a purge event that was used to tune the value of τ_p of Equation (19).

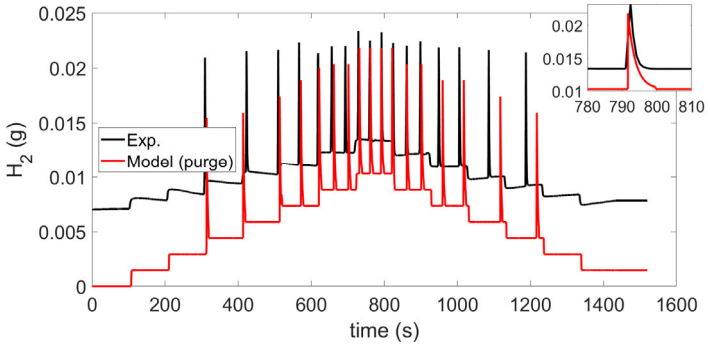

Figure 18. Tuning of the purge model by means of the H_2 mass flow rate signal (repetition 1, test C1).

Table 8 presents the results of applying the purge model to the remaining tests. Despite the inherent challenges in accurately replicating the complex purge logic, the model effectively captures the operation of the purge valve, as evidenced by its correct prediction of the total number of purge spikes across the different test scenarios.

Table 8. Validation of the urge model: number of spikes.

Test Signal	Number of Repetitions	Experimental	Model
C0	1	10	12
C1	9	17	16
C2	1	17	19
C3	1	15	15

5. Results of the Application to the UAV Case

This section shows how the model can be applied practically to correct the estimation of hydrogen consumption in a drone. In particular, the effect of purge, SCU, and altitude are addressed.

Figure 19 compares the cumulative curves of hydrogen consumption calculated with Equation (18) with purge only (green line) with both purge and SCU (red dotted line) and

shows the corrected flight time (red square). While the effect of purge is evident, the action of the SCU has a limited impact on the estimation of fuel consumption. In relative terms, the purge increases the estimated consumption by 4.8%. The additional effect of the SCU brings +5.6% more hydrogen consumption, compared with the theoretical value obtained from Equation (18). This capability is of practical relevance, since the consumption of H_2 is directly associated with the flight time of the drone.

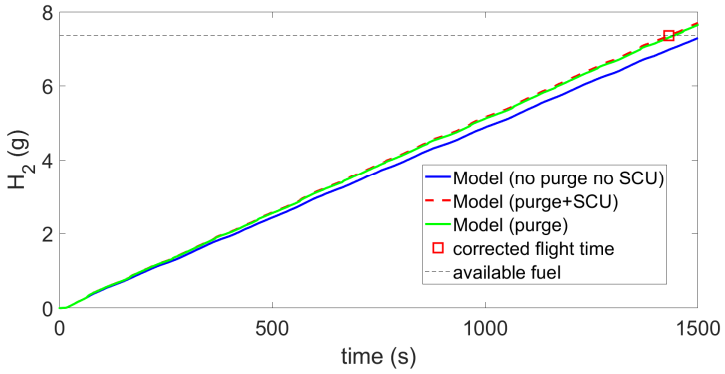

Figure 19. Effect of purge and SCU on cumulative H_2 mass consumption (flight test with SCU on).

The model allows for a more comprehensive estimation of hydrogen consumption than the simple application of Equation (18) used in the scientific literature and, therefore, a more correct quantification of the UAV's endurance. Assuming the drone is equipped with a tank containing exactly 7.4 g of hydrogen (as per stoichiometric calculation), it would not be able to complete the 25 min flight, as it would run out of hydrogen after about 24 min (−4.5%). The procedure for determining the corrected flight time is illustrated in Figure 19. Note that the penalty, in terms of additional fuel consumption, relies on a purge and short-circuit valve model that lacks full validation due to mass flow rate measurement drift. Nevertheless, this limitation does not undermine the key reasoning: accurately estimating hydrogen consumption remains critical.

Another relevant trait of the proposed model is the possibility to estimate the effect of altitude on the performance of the fuel cell. To put into evidence this feature, the model was run with a constant current of 10 A but with an increasing altitude up to 1000 m with ramps of 100 s, waiting for 300 s so that the stack could reach a steady-state operation. The inputs and main outputs of the simulation are shown in Figure 20.

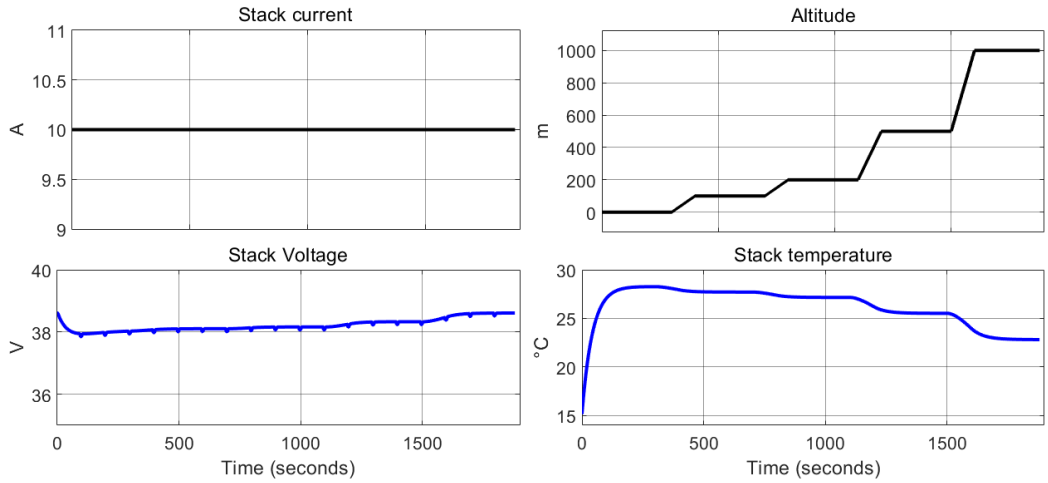

Figure 20. Input (**top**) and main output (**bottom**) of the simulation, with variable altitude and constant stack current (sea-level-tuned fan control).

Results indicate that, after a short decrease in the first 50 s due to the delay in reaching the steady-state temperature at sea level, the stack voltage shows an increase with altitude. This result is apparently in contrast with the scientific literature described in the introduction, and, in particular, with the experimental and numerical results of Xiao et al. [43], but it can be explained by the behavior of the stack temperature.

If the stack temperature is kept constant through an appropriate control strategy, as in liquid-cooled stacks, the cell voltage decreases with altitude. This behavior results from the reduction in oxygen partial pressure, which lowers the term E_1 of the Nernst voltage, Equation (4), and increases activation losses, Equation (8), through the exchange current (see Figure 21). In particular, the Nernst voltage at 2000 m is reduced by 1.9 mV per cell because of the reduced oxygen partial pressure if the stack temperature was kept constant at 34 °C (steady-state value at 10 A, according to Figure 12). Moreover, the increase in altitude reduces the mass flow rate of the fans because of the reduced air density, with a negative effect on the fan's parasitic power. In this study, the stack temperature decreases with altitude because the fan control strategy depends solely on the current and does not compensate for the lower air temperature and density [32]. The details of the Nerst voltage, activation losses, and cell voltage in the two cases (constant temperature and sea-level-tuned fan control) are compared in Figure 21. The negative spikes are due to the reduction in oxygen partial pressure during the purge.

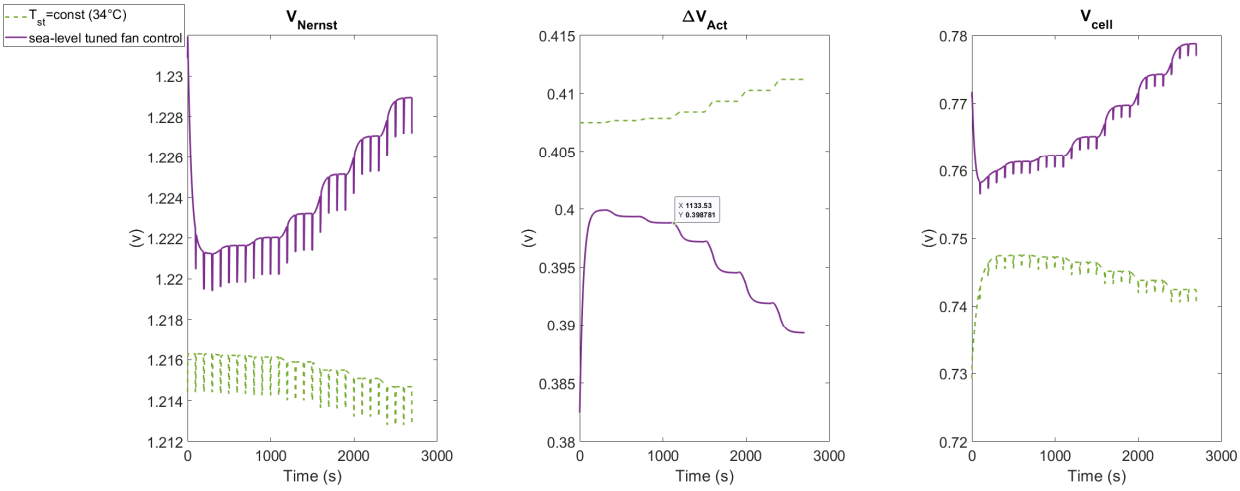

Figure 21. Effect of altitude on the cell voltage (constant stack temperature vs. sea-level-tuned fan control).

Figure 22 shows the balance between generated and exchanged heat through forced convection, natural convection, and latent heat. After an initial increase due to the start-up of the cell, the temperature decreases with altitude because of the colder ambient temperature that counterbalances the reduction in mass flow rate due to the reduced density and determines slight increases in both the forced and natural convection. In turn, the decrease in temperature increases the stack voltage and reduces the generated heat, fostering the temperature reduction. The improvement of the voltage is mainly due to the increase in term E_0 of the Nernst voltage, Equation (3), with altitude, due to the improved Gibbs free energy (reduced reaction entropy). In other words, the dominant effect on E_{Nernst} and, consequently, V_{st}, is correlated with the improved thermodynamic efficiency [39].

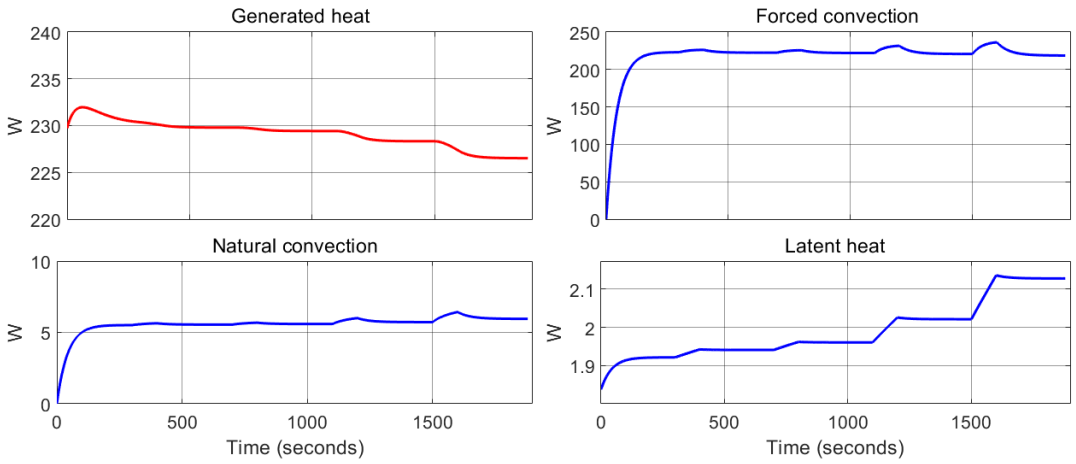

Figure 22. Details of the effect of altitude on the thermal balance for the altitude simulated test (sea-level-tuned fan control).

Note that the stack temperature is always significantly lower than 34 °C, which is the set point for the temperature in steady-state operation at 10 A. This continuous operation at a low temperature can have a negative impact on the FC lifespan, as pointed out by [33], because it can create durability and water-management problems, which are not yet addressed in the proposed model.

This result underlines the need to implement more advanced fan speed control methods for altitude operation. This further investigation will be performed after completing validation of the model by repeating the tests in the altitude chamber. In fact, other parameters like the amount of hydrogen lost through the purging valve are expected to be affected by altitude.

6. Model Limitations

Despite the satisfactory agreement with the experimental data, several limitations remain in the present formulation of the dynamic model. These aspects will be addressed in future developments of the work.

First, membrane hydration is not explicitly modeled. Ohmic resistance is treated as a constant parameter, with two discrete values to distinguish operation with and without SCU activation. Since ionic conductivity is strongly dependent on membrane water content, this simplification limits the accuracy of the model under rapid humidity variations and partially explains the discrepancies observed during the dynamic tests.

Second, the representation of the purge valve and SCU is based on simplified state-machine logics and an exponential evolution of the associated hydrogen spikes. Although this approach reproduces the correct timing and magnitude of the purge and short-circuit events, it does not resolve the underlying water-transport phenomena, impurity accumulation, or catalyst-surface effects. Consequently, the voltage recovery and degradation mechanisms associated with repeated SCU operation cannot be fully captured.

Another important limitation is related to humidity observability. Since neither the cathode's relative humidity nor the membrane water balance can be measured on the tested system, all humidity-related effects remain embedded in fitted parameters, preventing a detailed analysis of water-management behavior under extreme ambient conditions.

The model validation is also affected by the uncertainty of the hydrogen flowmeter, which exhibited a drift—particularly at low load—during the experimental campaign. Although the model correctly predicts the frequency and magnitude of the purge-induced spikes, the comparison of absolute hydrogen consumption must be considered with caution. This issue will be addressed with the new flowmeter installed in the altitude chamber.

Furthermore, the fan model neglects the dynamic response of the motor and relies on steady-state correlations between the current and rotational speed. Altitude effects are accounted for only through air-density correction, without using full fan performance maps. This simplification may lead to deviations during rapid load or altitude transients, where pressure effects become relevant.

Finally, the present model does not include a detailed degradation module and cannot be used to assess long-term aging phenomena such as catalyst deterioration, membrane thinning, or carbon corrosion. In addition, the altitude effects discussed in Section 5 have not yet been experimentally validated, since the tests in the altitude chamber are still pending. A complete validation under controlled temperature, humidity, and pressure conditions is therefore required to refine several sub-models, including purge behavior, SCU dynamics, and thermal management at a low air density.

7. Conclusions

This work presents a comprehensive dynamic model of a 1 kW open-cathode PEM fuel cell system, including the full balance of plant and the control logic for the cooling fans, purge valve, and short-circuit unit. The model was validated through an extensive experimental campaign that included stepwise, triangular, and UAV-derived load profiles, demonstrating its capability to accurately reproduce the coupled electrical, thermal, and reactant-management dynamics of the system.

A key outcome of this study is the quantitative assessment of hydrogen losses associated with purging and short-circuit events during realistic UAV operation. For a representative 25 min flight mission, the model predicts that purge-induced hydrogen losses increase total consumption by approximately 4.8%, while the additional contribution of the SCU raises the increase to 5.6%. Although these predictions are yet to be fully validated, they highlight the critical importance of explicitly accounting for balance of plant (BOP)-related losses when estimating endurance or sizing hydrogen storage for UAVs.

The model was also applied to explore the effects of altitude under controlled operating conditions. Results indicate that when the fan control strategy relies solely on the stack current, the decrease in ambient temperature with altitude outweighs the impact of the reduced air density, resulting in an overall lowering of the stack temperature. This temperature drop leads to an increase in cell voltage due to improved thermodynamic efficiency. While consistent with recent observations for open-cathode stacks, this finding underscores the need to develop more advanced temperature-control strategies for high-altitude flight to avoid prolonged operation at excessively low stack temperatures, which can accelerate membrane degradation.

While the coupled model effectively captures the interplay among voltage, temperature, and fan speed, there is room for improvement. Specifically, refining the thermal convection coefficients and certain voltage model terms will enhance the predictive accuracy. Further project work will focus on detailed modeling of critical phenomena, such as membrane hydration effects on ohmic resistance, and on developing advanced control strategies for cooling fans, the purge valve, and the short-circuit unit. These enhancements are expected to improve the model's fidelity and enable better design and control optimization for dynamic fuel cell operation.

Overall, the proposed model provides a robust and comprehensive tool for analyzing the transient behavior of open-cathode PEMFC systems and for evaluating the impact of operating strategies, ambient conditions, and UAV mission profiles. This comprehensive dynamic model advances sustainable aviation by enabling precise quantification of balance of plant losses and altitude effects in open-cathode PEMFCs, directly supporting the transition to zero-emission UAV propulsion. By optimizing hydrogen utilization—reducing

purge- and SCU-related waste by up to 5.6%, relative to stoichiometry—the model facilitates extended flight endurance with a minimal environmental footprint, aligning with SDG 7 (affordable and clean energy) and SDG 13 (climate action). These validated insights provide a foundational tool for designing efficient hybrid powertrains that minimize lifecycle emissions and resource consumption in low-carbon aerial applications.

Future work will include a complete validation under controlled altitude conditions using the dedicated altitude chamber, refined modeling of membrane hydration and SCU dynamics, and the integration of optimized fan-control strategies to further enhance high-altitude performance and prolong fuel cell lifetime.

Author Contributions: Conceptualization, T.D.; methodology, T.D.; software, T.D.; validation, T.D. and A.G.B.; investigation, A.F.; resources, T.D. and A.G.B.; data curation, T.D. and A.G.B.; writing—original draft preparation, T.D. and A.G.B.; writing—review and editing, T.D. and A.F.; supervision, T.D.; project administration, A.F.; funding acquisition, A.F. All authors have read and agreed to the published version of the manuscript.

Funding: This research was supported by the project SCIAME—Smart City Integrated Air Mobility Evolution (code F/310305/01-05/X56, CUP. B99J23000370005), funded by the "Partnerships for Innovation" program of the Italian Ministry of Enterprises and Made in Italy. The experimental research activity was founded by the Department of Engineering for Innovation at the University of Salento, with resources provided by the Italian Ministry of University and Research, Art. 238, paragraph 5 of Decree-Law No. 34 of 19 May 2020 (converted with amendments by Law No. 77 of 17 July 2020).

Informed Consent Statement: Not applicable.

Data Availability Statement: Data available upon request.

Acknowledgments: The authors would like to thank DTA-Scarl (regional district for aeronautics) for the acquisition of the experimental data on the quadcopter and Antonio Masciullo of the Department of Engineering for Innovation, for the help in setting up the experimental testbed for the fuel cell.

Conflicts of Interest: The authors declare no conflicts of interest.

Symbols and Abbreviations

$c_{P.air}$	Specific heat capacity of air
C_{FC}	Specific heat capacity of the stack
E_{Nernst}	Nernst voltage
E_0	Available voltage
E_1	Correction to E_{Nernst} for reactants' partial pressure
E_d	Correction to E_{Nernst} for dynamic effects
F	Faraday constant
h_{nat}	Natura convection heat transfer coefficient
I_{max}	Limit current of the stack
I_{st}	Stack current
$i*$	Corrected current for concentration losses
I_0	Exchange current
k	Empirical coefficient in dynamic correction
k_w	Empirical coefficient for sensible and latent heat
k_{SC}	SCU-related degradation coefficient
L_w	Latent heat of vaporization
m_{FC}	Stack mass
$\dot{m_{air}}$	Air mass flow rate
M_{H2}	Hydrogen molar mass
$\dot{m}_{H_2}$	Hydrogen mass flow rate

$\dot{m}_{H_2,react}$	Hydrogen mass flow consumed in reaction
$\dot{m}_{H_2,max}$	Maximum purge mass flow
n_{fan}	Fan speed
N	Number of cells in series
P_a	Anode pressure
P_{amb}	Ambient pressure
P_c	Cathode pressure
P_{fan}	Fan's parasitic power
P_{gross}	Gross stack power
P_{net}	Net power of the fuel cell system
P_{H_2}	Hydrogen partial pressure
P_{N2}	Nitrogen partial pressure
P_{net}	Net power of the fuel cell system
P_{O2}	Oxygen partial pressure
P_w^{sat}	Saturation vapor pressure for water
$\dot{Q}_{sens+lat}$	Sensible and latent heat loss
$\dot{Q}_{l/g}$	Latent heat loss
$\dot{Q}_{fan}$	Forced convection heat loss
$\dot{Q}_{gen}$	Reaction heat generation
$\dot{Q}_{nat}$	Natural convection heat loss
$\dot{Q}_{rad}$	Radiative heat loss
R	Universal gas constant
R_{Ohm}	Ohmic resistance
RH	Relative humidity
S_{act}	Activation area of the stack
S_{nat}	Heat-transfer area of the stack
T_{amb}	Ambient temperature
T_{st}	Stack temperature
t	Time
t_1	Start time of purge interval
t_p	Purge period
t_s	Short circuit period
Δt_{open}	Purge open valve interval
Δt_{SCU}	Short circuiting interval
UF	Hydrogen utilization factor
ΔV_{act}	Activation overpotential
ΔV_{conc}	Concentration overpotential
ΔV_{SCU}	Voltage drop due to impurity accumulation
ΔV_{ohm}	Ohmic overpotential
V_c	Cell voltage
V_{st}	Stack voltage
z	Altitude
α	Charge transfer coefficient
β	Concentration losses fitting parameter
η_{net}	Net efficiency of the fuel cell system
η_{vol}	Voltage efficiency of the cell
λ	Evaporation factor
λ_{din}	Constant factor for E_d
ρ_a	Air density
$\rho_{(s.l.)}$	Air density at sea level
ρ_w	Water density
τ_e	Overall flow delay
τ_p	Purge time constant

The following abbreviations are used in this manuscript:

BOP	Balance of Plant
FCS	Fuel Cell System
ISA	International Standard Atmosphere
LHV	Lower Heating Value
PEMFC	Proton Exchange Membrane Fuel Cell
SCU	Short-Circuit Unit
SDG	Sustainable Development Goals
s. l.	Sea Level

References

1. Yusaf, T.; Fernandes, L.; Abu Talib, A.R.; Altarazi, Y.S.M.; Alrefae, W.; Kadirgama, K.; Ramasamy, D.; Jayasuriya, A.; Brown, G.; Mamat, R.; et al. Sustainable Aviation—Hydrogen Is the Future. *Sustainability* **2022**, *14*, 548. [CrossRef]
2. Gu, Y.; Wiedemann, M.; Ryley, T.; Johnson, M.E.; Evans, M.J. Hydrogen-Powered Aircraft at Airports: A Review of the Infrastructure Requirements and Planning Challenges. *Sustainability* **2023**, *15*, 15539. [CrossRef]
3. Xu, L.; Huangfu, Y.; Ma, R.; Xie, R.; Song, Z.; Zhao, D.; Yang, Y.; Wang, Y.; Xu, L. A Comprehensive Review on Fuel Cell UAV Key Technologies: Propulsion System, Management Strategy, and Design Procedure. *IEEE Trans. Transp. Electrif.* **2022**, *8*, 4118–4139. [CrossRef]
4. Xiao, C.; Wang, B.; Zhao, D.; Wang, C. Comprehensive investigation on Lithium batteries for electric and hybrid-electric unmanned aerial vehicle applications. *Therm. Sci. Eng. Prog.* **2023**, *38*, 101677. [CrossRef]
5. Squadrito, G.; Maggio, G.; Passalacqua, E.; Lufrano, F.; Patti, A. An empirical equation for polymer electrolyte fuel cell (PEFC) behaviour. *J. Appl. Electrochem.* **1999**, *29*, 1449–1455. [CrossRef]
6. Zhang, C.; Liu, H.; Zeng, T.; Chen, J.; Lin, P.; Deng, B.; Liu, F.; Zheng, Y. Systematic study of short circuit activation on the performance of PEM fuel cell. *Int. J. Hydrogen Energy* **2021**, *46*, 23489–23497. [CrossRef]
7. Larmine, J.; Dicks, A. *Fuel Cell Systems Explained*; Wiley: Hoboken, NJ, USA, 2003, ISBN 9780470848579.
8. Niu, T.; Yu, X.; Zhang, C.; Wang, G.; Han, M.; Liu, H.; Zhao, F.; Shuai, Q. Purge Strategy Analysis of Proton Exchange Membrane Fuel Cells Based on Experiments and Comprehensive Evaluation Method. *Fuel* **2024**, *363*, 130970. [CrossRef]
9. Munsi, M.S.; Joshi, R.P. Comprehensive Analysis of Fuel Cell Electric Vehicles: Challenges, Powertrain Configurations, and Energy Management Systems. *IEEE Access* **2024**, *12*, 145459–145482. [CrossRef]
10. Strahl, S.; Husar, A.; Puleston, P.; Riera, J. Performance Improvement by Temperature Control of an Open-Cathode PEM Fuel Cell System. *Fuel Cells* **2014**, *14*, 466–478. [CrossRef]
11. Bradley, T.H.; Moffitt, B.A.; Mavris, D.N.; Parekh, D.E. Development and experimental characterization of a fuel cell powered aircraft. *J. Power Sources* **2007**, *171*, 793–801. [CrossRef]
12. Trogadas, P.; Cho, J.I.; Kapil, N.; Rasha, L.; Corredera, A.; Brett, D.J.; Coppens, M.O. Effect of extended short-circuiting in proton exchange membrane fuel cells. *Sustain. Energy Fuels* **2020**, *4*, 5739–5746. [CrossRef]
13. Kim, J.; Kim, D.M.; Kim, S.Y.; Nam, S.W.; Kim, T. Humidification of polymer electrolyte membrane fuel cell using short circuit control for unmanned aerial vehicle applications. *Int. J. Hydrogen Energy* **2014**, *39*, 7925–7930. [CrossRef]
14. Harel, F.; Gustin, F.; Mainka, J.; Wu, P. Effects of short circuit applications on PEM fuel cell performance and degradation. *J. Power Sources* **2025**, *632*, 236348. [CrossRef]
15. Zhao, D.; Xia, L.; Dang, H.; Wu, Z.; Li, H. Design and control of air supply system for PEMFC UAV based on dynamic decoupling strategy. *Energy Convers. Manag.* **2022**, *253*, 115159. [CrossRef]
16. Peng, H.; Stefanopoulou, A.G. Simulation and analysis of transient fuel cell system performance-based on a dynamic reactant flow model. In Proceedings of the IMECE'02, ASME International Mechanical Engineering Congress & Exposition, New Orleans, LA, USA, 17–22 November 2002.
17. Kandidayeni, M.; Macias, A.; Amamou, A.; Boulon, L.; Kelouwani, S.; Chaoui, H. Overview and benchmark analysis of fuel cell parameters estimation for energy management purposes. *J. Power Sources* **2018**, *380*, 92–104. [CrossRef]
18. Sun, L.; Jin, Y.; You, F. Active disturbance rejection temperature control of open-cathode proton exchange membrane fuel cell. *Appl. Energy* **2020**, *261*, 114381. [CrossRef]
19. Hu, M.; Zhao, R.; Pan, R.; Cao, G. Disclosure of the internal mechanism during activating a proton exchange membrane fuel cell based on the three-step activation method. *Int. J. Hydrogen Energy* **2021**, *46*, 3008–3021. [CrossRef]
20. Zhan, Y.; Guo, Y.; Zhu, J.; Liang, B.; Yang, B. Comprehensive influences measurement and analysis of power converter low frequency current ripple on PEM fuel cell. *Int. J. Hydrogen Energy* **2019**, *44*, 31352–31359. [CrossRef]
21. Tan, B.; Chen, H.; Quan, R.; Quan, S.; Zhou, Y. Study on data-driven PEMFC humidity mechanism soft-sensing model. *J. Phys. Conf. Ser.* **2019**, *1423*, 012043. [CrossRef]

22. Guzzella, L.; Sciarretta, A. *Vehicle Propulsion Systems, Introduction to Modeling and Optimization*, 3rd ed.; Springer: Berlin/Heidelberg, Germany, 2013.
23. Ren, P.; Pei, P.; Li, Y.; Wu, Z.; Chen, D.; Huang, S. Degradation mechanisms of proton exchange membrane fuel cell under typical automotive operating conditions. *J. Prog. Energy Combust. Sci.* **2020**, *80*, 100859. [CrossRef]
24. Wang, C.; Nehrir, M.; Shaw, S. Dynamic Models and Model Validation for PEM Fuel Cells Using Electrical Circuits. *IEEE Trans. Energy Convers.* **2005**, *20*, 442–451. [CrossRef]
25. Restrepo, C.; Konjedic, T.; Garces, A.; Calvente, J.; Giral, R. Identification of a Proton-Exchange Membrane Fuel Cell's Model Parameters by Means of an Evolution Strategy. *IEEE Trans. Ind. Inform.* **2015**, *11*, 548–559. [CrossRef]
26. Boukoberine, M.N.; Zia, M.F.; Benbouzid, M.; Zhou, Z.; Donateo, T. Hybrid fuel cell powered drones energy management strategy improvement and hydrogen saving using real flight test data. *Energy Convers. Manag.* **2021**, *236*, 113987. [CrossRef]
27. Boukoberine, M.N.; Donateo, T.; Benbouzid, M. Optimized energy management strategy for hybrid fuel cell powered drones in persistent missions using real flight test data. *IEEE Trans. Energy Convers.* **2022**, *37*, 2080–2091. [CrossRef]
28. Shuhayeu, P.; Martsinchyk, A.; Martsinchyk, K.; Milewski, J. Investigating PEM Fuel Cells as an Alternative Power Source for Electric UAVs: Modeling, Optimization, and Performance Analysis. *Energies* **2024**, *17*, 4427. [CrossRef]
29. Hyun, D.; Han, J.; Hong, S. Development of hybrid-powered, sustainable multi-purpose drone system: An analysis model. *Int. J. Hydrogen Energy* **2024**, *61*, 762–773. [CrossRef]
30. Donateo, T. Simulation Approaches and Validation Issues for Open-Cathode Fuel Cell Systems in Manned and Unmanned Aerial Vehicles. *Energies* **2024**, *17*, 900. [CrossRef]
31. Atkinson, R.W.; Hazard, M.W.; Rodgers, J.A.; Stroman, R.O.; Gould, B.D. An Open-Cathode Fuel Cell for Atmospheric Flight. *J. Electrochem. Soc.* **2017**, *164*, F46–F54. [CrossRef]
32. Mus, J.; Nuyttens, R.; Vanierschot, M.; Vandeginste, V.; Buysschaert, F. Experimental study of the effects of ambient conditions on the performance of open-cathode PEM fuel cells. *J. Power Sources* **2025**, *660*, 238467. [CrossRef]
33. Mus, J.; Nuyttens, R.; Vanierschot, M.; Vandeginste, V.; Buysschaert, F. A review of the impact of ambient conditions and degradation in hybrid fuel cell powered unmanned aerial vehicles. *J. Power Sources* **2024**, *624*, 235571. [CrossRef]
34. Ishaku, J.; Lotfi, N.; Zomorodi, H.; Landers, R.G. Control-oriented modeling for open-cathode fuel cell systems. In Proceedings of the 2014 American Control Conference—ACC 2014, Portland, OR, USA, 4–6 June 2014; pp. 268–273.
35. Mahjoubi, C.; Olivier, J.C.; Skander-Mustapha, S.; Machmoum, M.; Slama-Belkhodja, I. An improved thermal control of open cathode proton exchange membrane fuel cell. *Int. J. Hydrogen Energy* **2019**, *44*, 11332–11345. [CrossRef]
36. Sun, L.; Shen, J.; Hua, Q.; Lee, K.Y. Data-driven oxygen excess ratio control for proton exchange membrane fuel cell. *Appl. Energy* **2018**, *231*, 866–875. [CrossRef]
37. Li, Q.; Chen, W.; Wang, Y.; Liu, S.; Jia, J. Parameter identification for PEM fuel-cell mechanism model based on effective informed adaptive particle swarm optimization. *IEEE Trans. Ind. Electron.* **2010**, *58*, 2410–2419. [CrossRef]
38. Pratt, J.W.; Brouwer, J.; Samuelsen, G.S. Performance of proton exchange membrane fuel cell at high-altitude conditions. *J. Propuls. Power* **2007**, *23*, 197–203. [CrossRef]
39. Mohamed, W.W.; Kamil, M.H.M. Hydrogen preheating through waste heat recovery of an open-cathode PEM fuel cell leading to power output improvement. *Energy Convers. Manag.* **2016**, *124*, 543–555. [CrossRef]
40. Hou, Y.; Zhuang, M.; Wan, G. A transient semi-empirical voltage model of a fuel cell stack. *Int. J. Hydrogen Energy* **2007**, *32*, 857–862. [CrossRef]
41. Olivier, J.C.; Wasselynck, G.; Chevalier, S.; Auvity, B.; Josset, C.; Trichet, D.; Squadrito, G.; Bernard, N. Multiphysics modeling and optimization of the driving strategy of a light-duty fuel cell vehicle. *Int. J. Hydrogen Energy* **2017**, *42*, 26943–26955. [CrossRef]
42. Lin, Y.F.; Chen, Y.S. Experimental study on the optimal purge duration of a proton exchange membrane fuel cell with a dead-ended anode. *J. Power Sources* **2017**, *340*, 176–182. [CrossRef]
43. Xiao, C.; Wang, C.; Wang, B.; Yan, Y.; Cao, W. Model Predictive Energy Management for Open Cathode Fuel Cell and Battery Hybrid Power System Considering Effects of Varied Ambient Conditions in Unmanned Aerial Vehicle Applications. *SSRN*. 2024. Available online: https://papers.ssrn.com/sol3/papers.cfm?abstract_id=5332836 (accessed on 1 October 2025).